Accounting for Fabrication Variability in Transparent Perovskite Solar Cells for Four-Terminal Tandem Applications

Hu Quee Tan, Haoming Liang, Maximilian Krause, Xinhai Zhao, Radha Kothandaraman, Romain Carron, Ayodhya N. Tiwari, Fan Fu, Erik Birgersson,* Yi Hou,* and Hansong Xue*

Opto-electronic models that seek to predict the performance of perovskite and tandem solar cells (PSCs/TSCs) often keep the optical and recombination parameters (ORPs) constant in subsequent studies. During fabrication of PSCs, however, these parameters can vary significantly. To account for the inherent fabrication variability, a comprehensive opto-electronic-electric model to predict the current–voltage characteristics of four-terminal (4T) TSCs is developed. This model is calibrated with forty-eight in-house fabricated transparent PSCs with perovskite layer thickness of 420, 550, and 700 nm and corresponding median efficiencies of 20.6%, 21.1%, and 21.0%, respectively; a CIS bottom cell with stand-alone efficiency of 17.5%; and combined 4T TSCs with a median efficiency of 29.0%. After fitting and validation, the functional forms of the ORPs are captured to estimate how they change with perovskite layer thickness. Finally, the errors with models assuming constant ORPs are demonstrated and how to improve the TSCs efficiency to more than 30% is discussed.

H. Q. Tan, X. Zhao, E. Birgersson
Department of Mechanical Engineering
National University of Singapore
9 Engineering Drive 1, Singapore 117575, Singapore
E-mail: mpebke@nus.edu.sg

H. Q. Tan, H. Liang, X. Zhao, E. Birgersson, Y. Hou, H. Xue
Solar Energy Research Institute of Singapore (SERIS)
National University of Singapore
7 Engineering Drive 1, Singapore 117574, Singapore
E-mail: yi.hou@nus.edu.sg; xuehansong@u.nus.edu

H. Liang, Y. Hou
Department of Chemical and Biomolecular Engineering
National University of Singapore
4 Engineering Drive 4, Singapore 117585, Singapore

M. Krause, R. Kothandaraman, R. Carron, A. N. Tiwari, F. Fu
Laboratory for Thin Films and Photovoltaics Empa
Swiss Federal Laboratories for Materials Science and Technology
Ueberlandstrasse 129, 8600 Duebendorf, Switzerland

The ORCID identification number(s) for the author(s) of this article can be found under https://doi.org/10.1002/solr.202300339.

1. Introduction

A two-junction solar cell connects two solar cells electrically and mechanically in series as a two-terminal (2T) device or electrically decoupled as a four-terminal (4T) device. There are fewer design constraints for the latter as it does not require current matching to perform optimally. In addition, 4T tandem devices can perform better when operating conditions such as temperature and irradiance vary during operation.

In a tandem device, the transparent top solar cell typically has a wider bandgap than the bottom device and absorbs shorter wavelength light more efficiently than the bottom cell. The top device is relatively transparent to longer wavelength light, such as the infrared and visible light section of the solar spectrum, which is absorbed by the narrow-bandgap bottom cell. As the two subcells jointly absorb light more efficiently than a single-junction device, higher overall efficiency can be achieved. The perovskite solar cell is a potentially good candidate for the top cell in a tandem configuration as it can be tailored to have excellent optoelectronic properties—high absorption coefficient, high defect tolerance, and tunable bandgap. Good candidates for the bottom cell are solar cells made of silicon,[1–4] narrow bandgap perovskite,[5–8] CIS,[9,10] and CIGS.[11–14]

Several mathematical models have been developed and solved[15–26] to quantify and optimize the efficiency and optoelectronic properties of perovskite-based tandem devices. In these models, the optics are solved with either a one-dimensional transfer matrix method for tandem devices with planar interfaces[15–17,19,21,24–27] or with two-dimensional ray tracing for textured interfaces in the silicon bottom cell.[18,20,22] The current–voltage characteristics are modeled with either semiconductor physics[15–17,23–25] or equivalent circuits[19–22] for both subcells.

Some of these modeling studies quantified the optical losses in the perovskite cell[20,21] and mapped the measured optical constants for different bandgap perovskites to ensure current-matching conditions in a 2T configuration.[18] There are also modeling studies focusing on the operating conditions of the tandem device, such as quantifying the irradiance and temperature variations to the annual energy yield of the device[19] and

identifying the device architecture that is less sensitive to temperature variations.[15] Most of these modeling studies either quantified the optimal layer thickness for the different materials in the perovskite cell to achieve the highest device efficiency by varying one factor at a time (OFAT)[16,23,25,26,28] or through multiparametric optimization.[22,24,29] Common to all these modeling studies is the assumption that the material properties of the perovskite layer are independent of the perovskite layer thickness. However, there are experimental studies that have found the optical[30,31] and recombination[32,33] properties of the perovskite layer to vary with its layer thickness.

The main goal of this paper is to address the gap in accounting for the variability of the optical and recombination properties of the transparent perovskite top cell at different perovskite layer thicknesses when modeling a perovskite 4T tandem device. Here, the focus is on the perovskite top cell as it is a less mature technology than most of its bottom-cell counterparts. The performance of the perovskite cell is captured with a detailed opto-electronic model that considers the light propagation, charge-carrier electric field, and generation, recombination, and transport of charge carriers; the CIS bottom cell is modeled with a less detailed opto-electric model. By calibrating the opto-electronic-electric (OEE) model with the current–voltage characteristics from fabricated cells, we fit piecewise interpolating Hermite polynomials for the optical and recombination properties of the top perovskite cell that capture the inherent variability that arises in fabrication of perovskite solar cells—especially in the light-absorbing layer of the perovskite top cell.

2. Results and Discussion

In the following, we discuss the OEE model and its agreement with experimental perovskite/CIS 4T tandem-solar-cell efficiencies, fit polynomials for the optical and recombination properties of the perovskite cell, quantify how the optical and recombination properties vary with perovskite layer thickness, and compare how the results from optimizing the perovskite layer thickness differ from a model that assumes constant material properties.

2.1. Standalone and Tandem Devices

Typically, the perovskite layer thickness for semi-transparent perovskite solar cells ranges from 200 to 800 nm.[34,35] It has been found that for a 1.58 eV perovskite top cell, the optimal perovskite layer thickness for the top cell is 620 nm.[32] Thus, for our perovskite top cell with a bandgap of 1.63 eV, we narrow down the layer thickness range in this study to 420–700 nm.

A total of 48 perovskite top cells—16 cells each with 420, 550, and 700 nm perovskite layer thicknesses—and one CIS bottom cell were fabricated for a 4T tandem configuration to calibrate and validate the OEE model. Here, we focus on the perovskite layer thickness in the top cell as the key fabrication parameter as it affects the optical and recombination properties in a perovskite solar cell. The device architecture of the top cell is glass/ITO/NiO/Rb$_{0.05}$Cs$_{0.05}$[(FA$_{0.83}$MA$_{0.17}$)$_{0.9}$Pb(I$_{0.83}$Br$_{0.17}$)$_3$/C60/

Table 1. A summary of the median performance metrics for the semi-transparent standalone perovskite cells P$_{420}$, P$_{550}$, and P$_{700}$ with perovskite layer thicknesses of 420, 550, and 700 nm, respectively, and the standalone CIS cell.

Cell	Experiments				Simulated			
	i_{sc} [mA cm^{-2}]	V_{oc} [V]	$\mathfrak{I}$ [%]	η [%]	i_{sc} [mA cm^{-2}]	V_{oc} [V]	$\mathfrak{I}$ [%]	η [%]
P$_{420}$	20.6	1.22	78.7	19.73	20.7	1.23	77.7	19.85
P$_{550}$	21.1	1.23	81.0	21.01	21.2	1.25	77.9	20.60
P$_{700}$	21.0	1.22	75.9	19.48	21.1	1.22	74.8	19.40
CIS	40.4	0.6	72.5	17.54	40.4	0.6	72.3	17.52

SnO$_2$/ITO/LiF, and the bottom cell is MgF$_2$/AZO/ZnO/CdS/(Ag$_{0.1}$CuO$_{0.9}$)InSe$_2$/Mo/glass.

In stand-alone configuration, the three perovskite median cell efficiencies were measured as 19.73%, 21.01%, and 19.48%, as shown in **Table 1**, for perovskite layer thicknesses of 420, 550, and 700 nm, respectively, and the CIS cell achieved 17.54%.

In 4T tandem configuration, the reduced incident light on the CIS bottom cell results in an efficiency drop to 8.46%, 8.02%, and 7.72% for increasing layer thicknesses of the perovskite, as shown in **Table 2**. From the optical simulations, the top cell absorbs around 70% of the light in the 300–800 nm spectrum, which reduces the total light absorbed by the bottom cell by about 48% from the 300–1400 nm spectrum compared to its stand-alone configuration. In contrast, the measured top cell efficiencies did not change significantly from stand-alone to tandem configuration, because adding a bottom cell did not reflect significantly more light back into the top cell. This was seen in the optical simulation with a small increase of around 0.5% in the photogenerated current density of the top cell.

Overall, our tandem devices have relatively good performance: the tandem devices with a perovskite layer thickness of 550 nm achieved a median 29.03% efficiency as compared to the previously reported record of 27.1% tandem device with a similar device architecture.[10]

2.2. OEE Model

In our OEE model, shown schematically in **Figure 1**a, we solve for light propagation throughout the 4T tandem solar cell with the transfer-matrix method. In the top perovskite cell, we consider the electric field and charge-carrier generation, recombination, and transport with the energy band diagram shown in Figure 1b; and in the bottom CIS cell, a less detailed two-diode model is solved as shown in Figure 1c.

The more detailed model for the top cell is motivated by the fact that we focus on the perovskite top cell's fabrication design space in terms of the perovskite layer thickness. Furthermore, thin-film technologies such as the CIS have been in development since around 1975 as opposed to the more recent perovskite solar cells from around 2010. For the former, equivalent-circuit models such as the two-diode model have been shown to capture the current–voltage characteristic well.[36–38] In contrast, the equivalent circuit models for perovskite are not as well

Table 2. A summary of the median performance metrics for the CIS bottom cell CIS$_{420}$, CIS$_{550}$, and CIS$_{700}$ in tandem with perovskite layer thicknesses of 420, 550, and 700 nm, respectively, and the tandem cells.

| Cell	Experiments					Simulated				
	i_{sc} [mA cm^{-2}]	V_{oc} [V]	$\mathfrak{I}$ [%]	η [%]	η_{tot} [%]	i_{sc} [mA cm^{-2}]	V_{oc} [V]	$\mathfrak{I}$ [%]	η [%]	η_{tot} [%]
CIS$_{420}$	20.1	0.58	73.1	8.46		20.6	0.57	71.9	8.53	
CIS$_{550}$	19.2	0.57	72.9	8.02		19.9	0.57	72.0	8.20	
CIS$_{700}$	18.7	0.57	72.8	7.72		19.3	0.57	72.0	7.91	
P$_{420}$ + CIS$_{420}$					28.19					28.38
P$_{550}$ + CIS$_{550}$					29.03					28.8
P$_{700}$ + CIS$_{700}$					27.20					27.31
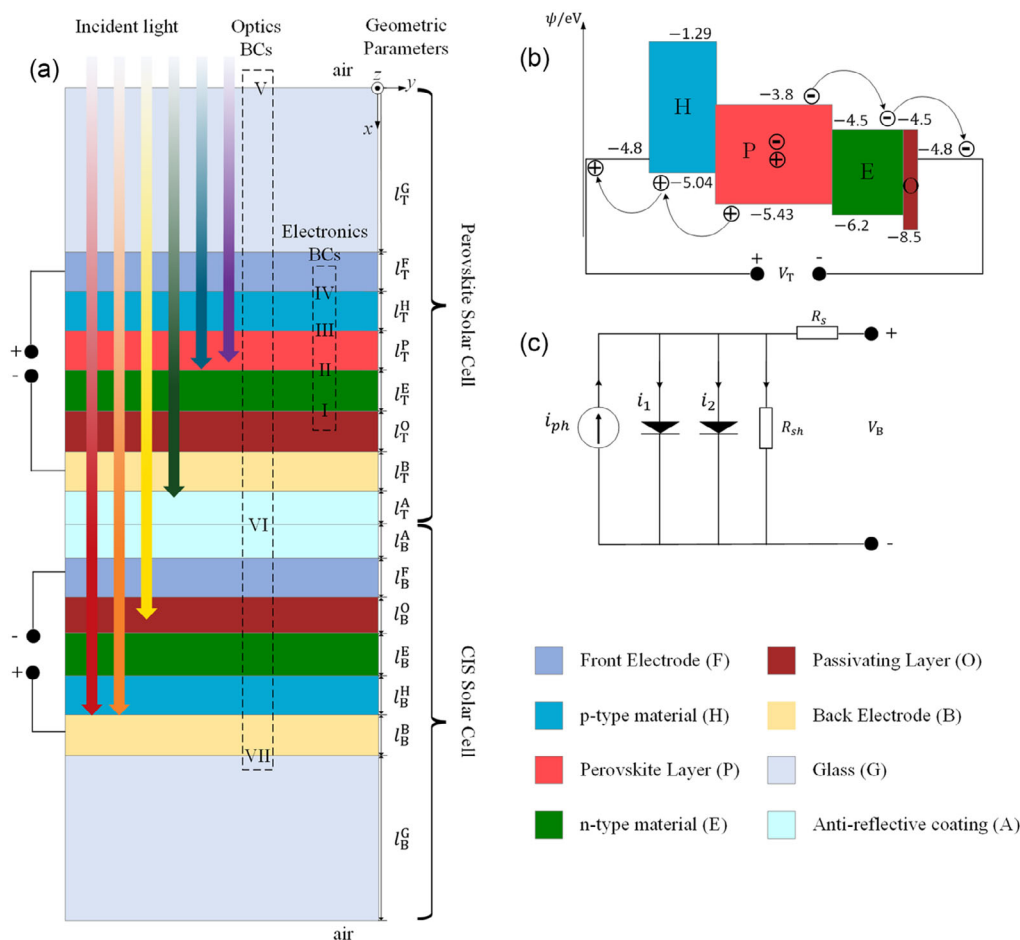
Figure 1. a) Schematic of a four-terminal perovskite on CIS tandem device. The Roman numerals denote the interfaces, l is the layer thickness, and the subscripts T and B denotes the top and bottom cell, respectively; b) the energy band diagram for the top perovskite cell; c) the equivalent circuit for the bottom CIS cell.

established and are not able to capture changes to the geometrical features and changes to the electronic properties such as electronic band structure and charge carrier mobilities. A direct benefit of combining a more detailed electronic model and a less detailed electric model is not only the reduced overall computational cost but also that we do not require as many input parameters for the electric model. In this context, we note that the

optics for the subcells are coupled, and we do not simulate a perovskite filter.

As shown in the fishbone diagram in **Figure 2**, the OEE model requires a total of 50 parameters—material properties, operating conditions, layer thicknesses—for the perovskite top cell and 28 parameters—material properties, layer thicknesses, resistances, ideality factors, saturation current densities and operating
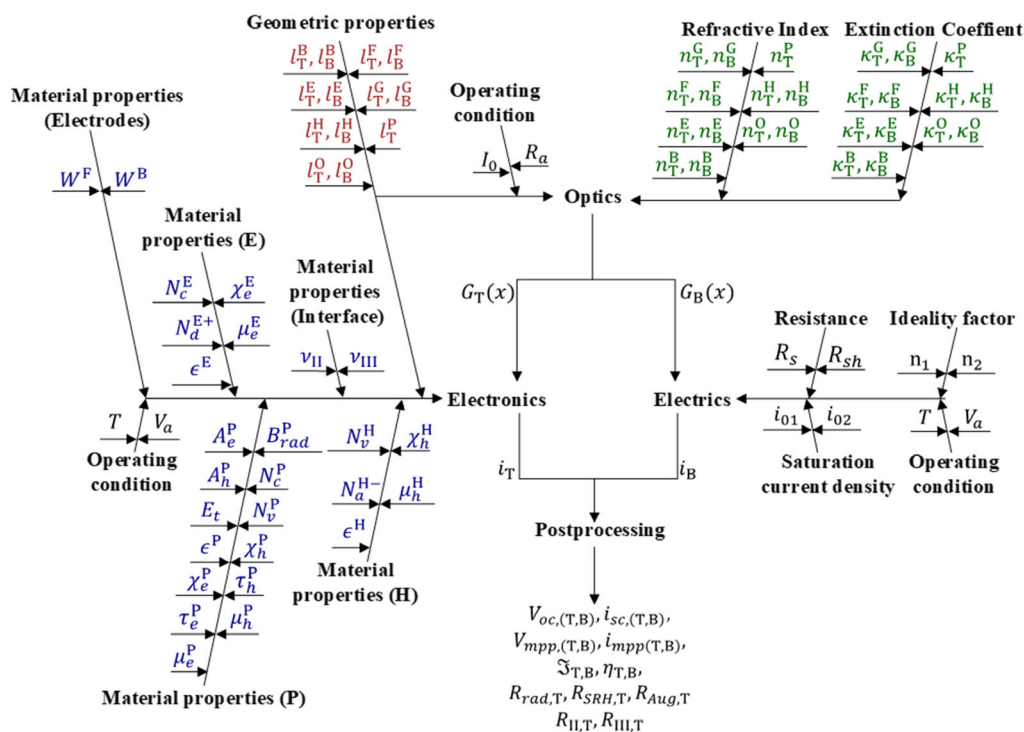
Figure 2. Input and output parameters for the OOE model. The electronics require the operating conditions, material properties, and thicknesses of all layers in the top cell as well as the charge carrier generation from the optics to predict the current–voltage characteristics of the top perovskite cell; the electrics require the resistances, saturation current densities, ideality factors, and operating conditions of the bottom cell as well as the average charge generation to predict the current–voltage characteristics of the bottom CIS cell, and the optics require the refractive indices, extinction coefficients, and thicknesses of all layers in the top and bottom cells to provide the charge generation in all cells. Postprocessing of the current–voltage characteristics yields the open-circuit voltage, short-circuit current, fill factor, efficiency, and the recombination losses.

conditions—for the CIS bottom cell. (For the sake of brevity, we refer the readers to the Nomenclature in Appendix for the definition of symbols and notations.) All parametric input values are summarized in **Table 3**.

2.3. Calibration and Validation

For the perovskite top cell, we determined the recombination parameters through a detailed analysis of the current–voltage characteristics of the standalone P_{420}, P_{550}, and P_{700} cells, as shown in **Figure 3**a–c. We employed the OEE model to fit the experimental data, which allowed us to determine the Auger, Shockley–Read–Hall (SRH), radiative, and interface recombination, along with the optical fitting parameter ξ. These parameters were used as fitting parameters to optimize the model's agreement with the experimental data. To ensure the accuracy of the fitting, we used genetic algorithm to minimize the difference between the experimental and simulated current–voltage curves.

For the bottom cell, we fitted the diode parameters using the current–voltage characteristics of the standalone CIS cell, as shown in Figure 3d. To validate the OEE model, we used the current–voltage characteristics of the bottom CIS_{420}, CIS_{550}, and CIS_{700} cells in the 4T configuration as shown in Figure 3e. Overall, we have good agreement between model predictions and experiments: the absolute errors of the efficiencies for the

standalone P_{420}, P_{550}, P_{700}, and the CIS cells are 0.12%, 0.41%, 0.08%, and 0.02%, respectively, and the absolute errors for the bottom CIS_{420}, CIS_{550} and CIS_{700} cell's efficiencies in the tandem configuration are 0.07%, 0.18%, and 0.19%, respectively. (Readers can find further details on the OEE model and its calibration and validation in the Experimental Procedures section.)

2.4. Fabrication Variability

The performance metrics—short-circuit current, open-circuit voltage, fill factor, and efficiency—for the 48 fabricated transparent perovskite top cells with three different layer thicknesses are depicted in **Figure 4**. Here, several features apparent: the metrics all display a maximum median around 550 nm, and the short-circuit currents vary from around 20 to 22 mA cm², the open-circuit voltages vary from around 1.21 to 1.24 V, the fill factors range from around 74 to 83%, and the efficiencies range from 18.84 to 21.46%.

In order to determine if the metrics are statistically different for the layer thicknesses, we first test if these cells have been drawn from normally distributed populations. A Lilliefors test reveals that the distributions for the metrics are normally distributed ($p > 0.05$) except for the efficiency ($p > 0.03$) and open-circuit voltage ($p > 0.049$) from the batch of perovskite solar cells

Table 3. Model parameters for single-junction PSC. Some of the parameters are fitted (fit) and estimated (est).

Parameters	Values	Units	References
Operating condition			
p_{in}	1000	W m^{-2}	
T	293	K	
Material properties			
A_e^P, A_h^P	Equation (5)	m^6 s^{-1}	Fit
B_{rad}^P	Equation (5)	m^3 s^{-1}	Fit
E_t	5.27	eV	Est[a]
N_a^{H-}, N_d^{E+}	0, 0	m^{-3}	Est[b]
$N_c^E, N_c^P, N_v^P, N_v^H$	$1 \times 10^{22}, 1 \times 10^{22}, 1 \times 10^{22}, 2 \times 10^{22}$	m^{-3}	[51–53]
W^F, W^B	4.8, 4.8	eV	[54]
$\chi_h^H, \chi_e^E, \chi_h^P, \chi_e^P$	5.04, 4.5, 3.8, 5.43	eV	[55–57]
$\varepsilon^H, \varepsilon^E, \varepsilon^P$	5.25 ε_0, 3.03 ε_0, 5.38 ε_0	F m^{-1}	Est[c], [58], Est[c]
$\mu_h^H, \mu_h^P, \mu_e^P, \mu_e^E$	$3.5 \times 10^{-5}, 3 \times 10^{-2}, 3 \times 10^{-2}, 1.6 \times 10^{-4}$	m^2 V^{-1} s^{-1}	[52,53,59]
τ_e^P, τ_h^P	Equation (5)	s	Fit
ν_{II}, ν_{III}	Equation (5)	m^4 s^{-1}	Fit
Geometrical properties			
l_T^G	1	mm	Est[d]
$l_T^F, l_B^F, l_T^H, l_B^H, l_T^P, l_T^E, l_B^E$	110, 225, 10, 2400, 420, 23,35	nm	Est[d]
$l_T^O, l_B^O, l_T^B, l_B^B, l_T^A, l_B^A$	10, 70, 110, 500, 100, 100	nm	Est[d]
Electrical properties			
i_{01}, i_{02}	$1.52 \times 10^{-8}, 1.73 \times 10^{-3}$	A m^{-2}	Fit
n_1, n_2	1, 2		
R_s, R_{sh}	$6.3 \times 10^{-5}, 0.179$	Ω m^2	Fit
Constants			
c	2.9979×10^8	m s^{-1}	
e	1.602×10^{-19}	C	
h	6.626×10^{-34}	J s	
k_B	1.38×10^{-23}	J K^{-1}	

[a]Perovksite from similar constituent materials;[60,61] [b]no additive added; [c]average taken from optics data; [d]SEM image.

with a 550 nm perovskite layer thickness. As there are both normal and non-normal distributions, we adopt the nonparametric Kruskal–Wallis test to determine if the medians of the performance metrics at the three thickness are statistically different. In our comparison, we found that the performance metrics of perovskite solar cells with a 420 nm perovskite layer thickness ($\overline{R}_\eta = 21.5$, $\overline{R}_{V_{oc}} = 17.1$, $\overline{R}_{\mathfrak{I}} = 25.3$, $\overline{R}_{i_{sc}} = 9.1$), 550 nm perovskite layer thickness ($\overline{R}_\eta = 40.5$, $\overline{R}_{V_{oc}} = 38.9$, $\overline{R}_{\mathfrak{I}} = 39.7$, $\overline{R}_{i_{sc}} = 33.5$), and 700 nm perovskite layer thickness ($\overline{R}_\eta = 11.5$, $\overline{R}_{V_{oc}} = 17.4$, $\overline{R}_{\mathfrak{I}} = 8.5$, $\overline{R}_{i_{sc}} = 30.9$) are statistically different ($H_\eta = 35.4$, $H_{V_{oc}} = 25.5$, $H_{\mathfrak{I}} = 39.8$, $H_{i_{sc}} = 29.4$), and we reject the null hypothesis that the effect on the performance metrics from the three perovskite layer thickness is the same ($p_\eta = 10^{-8}$, $p_{V_{oc}} = 10^{-6}$, $p_{\mathfrak{I}} = 10^{-9}$, $p_{i_{sc}} = 10^{-7}$). Post hoc pairwise comparison with the Dunn's test reveals that only the efficiency and open-circuit voltage of the perovskite solar cells with perovskite layer thickness of 420 and 700 nm (*p*-value > 0.05)

and the short-circuit current density of the perovskite solar cells with perovskite layer thickness of 550 and 700 nm (*p*-value > 0.05) are not statistically significant to conclude that they are different.

We now turn our attention toward the fitted parameters for the top and bottom cells, which are illustrated in **Figure 5**. The optical and recombination parameters are fitted with the champion, median, and the worst performing devices with piecewise cubic Hermite interpolating polynomials (see Experimental Section) to avoid overshoots.

In general, when the perovskite layer thickness increases, there is an increase in charge carrier generation and an increase in the distance for the charge carriers to reach the charge transport layers, resulting in an increase in bulk recombination.[33] From Figure 5b,c, the radiative recombination coefficient increases from 10^{-20} to 10^{-18} m^{3}s^{-1}, and the SRH lifetime decreases from 10^{-4} to 10^{-6} s when the perovskite layer thickness increases from 420 to 700 nm. As compared to the radiative
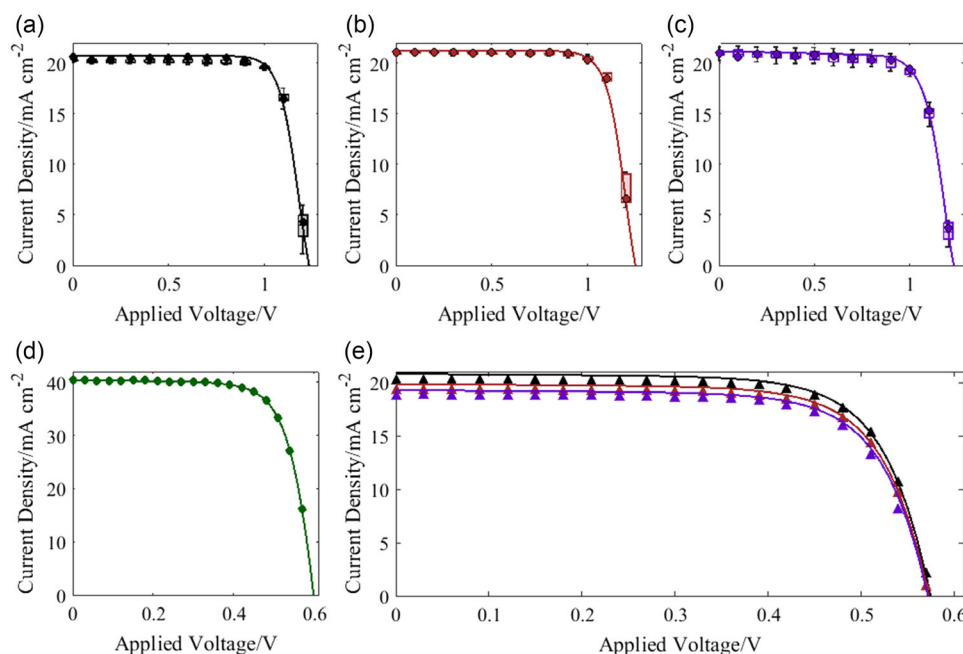
Figure 3. a–c) Current–voltage characteristics of the standalone top perovskite solar cell, d) standalone bottom CIS solar cell, and e) the bottom CIS cell in tandem configuration from experiments (•: calibration, ▲: validation, Boxplots) and model predictions (—). Here, the black, red, and purple color denote the subcell characteristics corresponding to the perovskite cell with perovskite layer thickness of 420, 550, and 700 nm, respectively; the green denotes the standalone CIS cell.
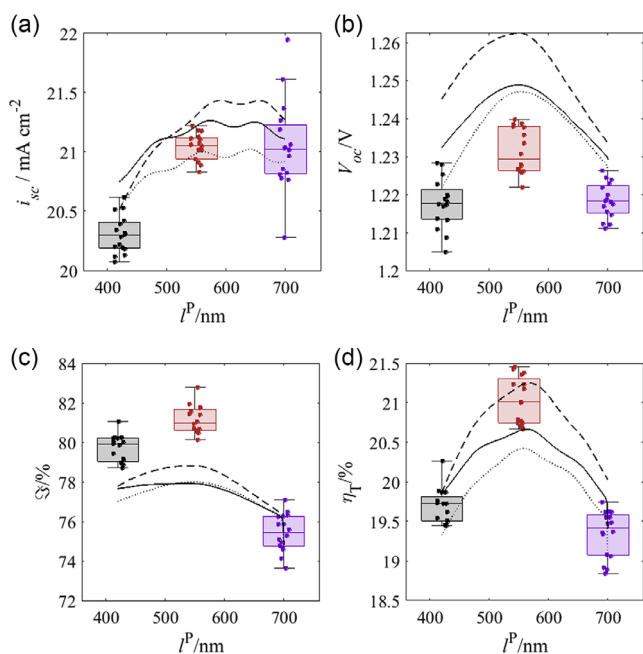
Figure 4. Comparison of a) short-circuit current density, b) open-circuit voltage, c) fill factor, and d) efficiency of the experimentally fabricated transparent perovskite subcell (•) and prediction from the OEE model from fitting the best (--), median (—) and worst (:) performing cell.

and SRH recombination, there is a less distinguishable trend for the Auger recombination, as shown in Figure 5a, which we attribute to the relatively small contribution of the Auger

recombination—around 3% to the bulk recombination at maximum power point.

Furthermore, it has been found that fabricating thicker perovskite layers can result in rougher perovskite surfaces, which in turn can lead to poorer conformity with the charge-carrier transport layers deposited on the rough surfaces, increasing the interfacial recombination at the interfaces.[39] Here, we note that the perovskite solar cell has a p-i-n configuration, and the perovskite layer was spin-coated on the hole-transporting layer (interface III) before the electron-transporting layer (interface II) is deposited onto the perovskite layer. In the remainder of the paper, we will be referring to the interface between the perovskite/electron-transporting layer as interface II and the interface between the perovskite/hole-transporting layer as interface III. As shown in Figure 5d, the interfacial recombination rate at interface II first decreases by around 20% when the perovskite layer thickness increases from 420 to 550 nm and then increases by around 200% as the layer thickness grows to 700 nm. This initial decrease followed by an increase suggests an improved conformity between the perovskite layer and the electron transport layer that then becomes poorer after around 550 nm.

In contrast, the interfacial recombination rate at interface III drops by around a factor of 2 when the perovskite layer thickness increases from 420 to 550 nm and remains relatively constant until a layer thickness of around 700 nm.

Finally, as depicted in Figure 5f, the fitting parameter, ξ, for the optics increases monotonically by up to an absolute 20% when the perovskite layer thickness increases from 420 to 700 nm. We refer the readers to the supporting information for the assumptions of the fitting parameter ξ and the optical
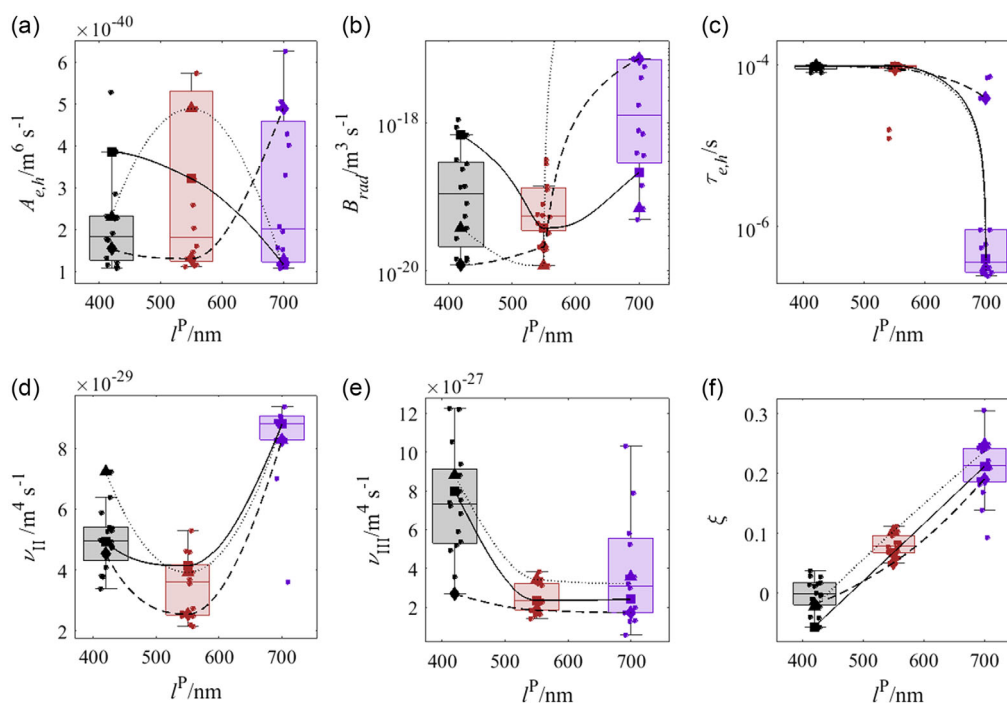
Figure 5. Fitted a) auger recombination coefficient, b) radiative recombination coefficient, c) Shockley–Read–Hall recombination lifetime, effective interface-recombination velocity at interface d) II and e) III, and f) fitting parameter ξ for the optics at different perovskite layer thickness. Here, we fit a functional form for the recombination and optical coefficients based on the best (--), median (—) and worst (:) performing cell from the experimental transparent perovskite top cells (♦: best, ■: median, ▲: worst performing and •: remaining cells).

properties of the perovskite layer. We attribute the increase in ξ with thicker perovskite layer thickness to the increase in perovskite crystal size when the perovskite layer thickness increases, resulting in a change in the optical constants of the perovskite layer.[31,32] With the poorer optical properties at thicker perovskite layer, we observe that the short-circuit current density for the perovskite solar cell increases from 20.3 to 21 mA cm^{-2} when the perovskite layer thickness increases from 420 to 550 nm before plateauing at around 21 mA cm^{-2} from 550 to 700 nm perovskite layer thickness.

Next, we determine how the recombination channels of the perovskite solar cell vary with the perovskite layer thickness at the maximum power point with the fitted optical and recombination coefficients. In the following discussion, unless stated otherwise, we will refer to the recombination current density to be at the maximum power point.

As compared to the interface recombination current density, the three bulk recombination current densities are 1–6 orders of magnitude smaller as shown in **Figure 6**. The distribution of the bulk recombination current densities is similar to the distribution of the fitted bulk recombination parameters, whereas there are clearer monotonically increasing and decreasing trends for the interface recombination at interfaces II and III, respectively. The interface recombination current density at interface II remains the dominant recombination mechanism, while when the perovskite layer thickness increases from 550 to 700 nm, the interface recombination current density at interface III falls from the second to third highest recombination channel, while

the SRH recombination current density moves up to the second place.

2.5. Comparison with Constant Material Properties

To contrast the difference in predicting the performance of a perovskite/CIS 4T tandem device with a model that accounts for fabrication variability and one that assumes constant material properties, we compare model predictions in **Figure 7**a–c for efficiencies of the top cell, bottom cell, and 4T tandem device. For the model with constant properties, the recombination coefficients and spectral optical constants were fitted with the current–voltage characteristics from the median experimental perovskite cell with a layer thickness of 550 nm, which is roughly in the middle of the experimental thickness interval.

As can be inferred from Figure 7a, the predictions are similar for perovskite layer thicknesses from 420 to 550 nm with a maximum absolute error of 0.25% before the results disagree significantly from 550 to 700 nm with a maximum absolute error of 2.16%. The model that accounts for the variability sees an increase in recombination and poorer absorption of light for the top cell and thus fewer charge carriers extracted from the active perovskite layer as compared with the model with constant parameters. Most importantly, the model with constant parameters does not capture the maximum at 21.3% around 550 nm and overpredicts the top cell and 4T tandem cell performance whilst underpredicting the performance of the bottom cell from
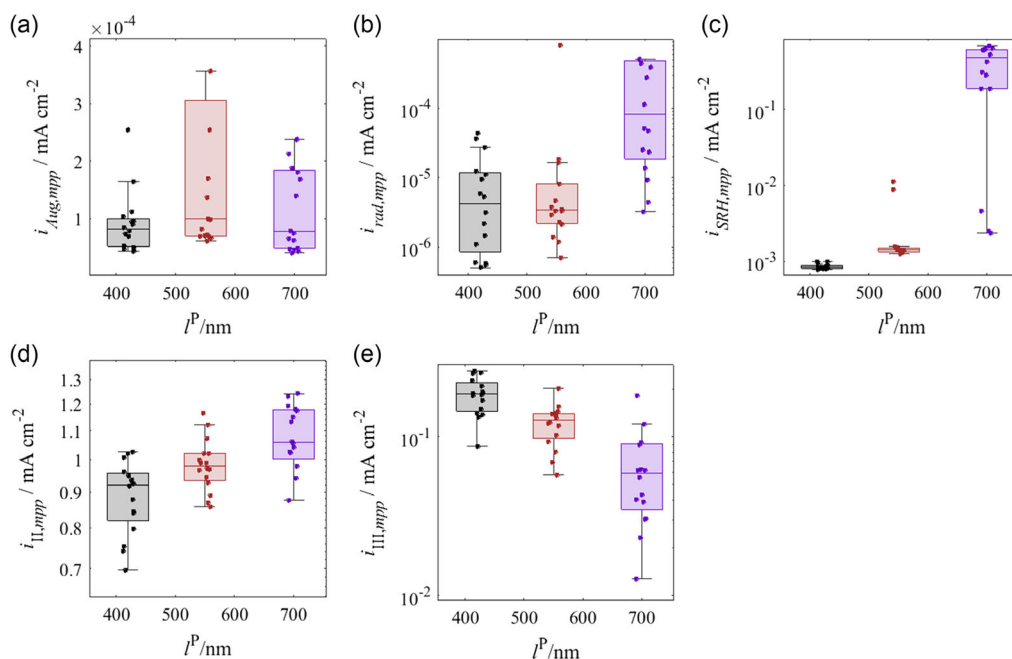
Figure 6. a) Statistics of Auger, b) radiative, c) SRH, d) interface II, and e) interface III recombination current density at maximum power point for perovskite cells with perovskite layer thickness of 420, 550, and 700 nm.
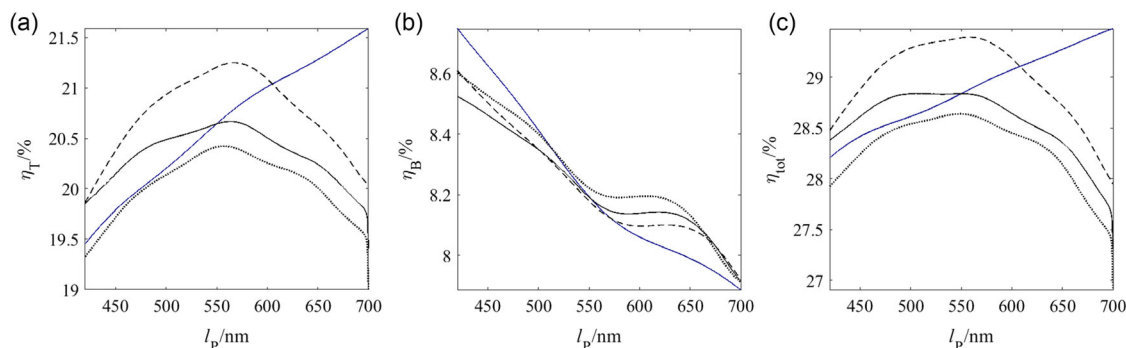
Figure 7. a) Top, b) bottom, and c) tandem device efficiency predicted from model accounting for fabrication variability with the best (--), median (—) and worst (:) performing cells, and model assuming constant material properties (—) at different perovskite layer thickness.

550 nm onward. In addition, the spread in efficiencies—here captured with the best, median, and worst cells—is not captured.

With the fitted OEE model, we carried out a multiparametric optimization of the layer thickness in the top perovskite cell, comprising of the front contact electrode, hole-transporting layer, perovskite layer, electron-transporting layer, and the back contact electrode. As shown in **Figure 8**, we can see the spread in the predicted optimal tandem efficiencies from the best, median, and worst-case scenario to be at 30.3%, 29.8%, and 29.4%, respectively. The results predict the optimal perovskite layer thickness to remain around 550 nm, while the most noticeable changes in the optimal configuration are the reduction of the electron transport layer from 23 to around 12 nm and a reduction of the back contact electrode from 110 to 100 nm to further improve the top and bottom subcell efficiencies.

3. Conclusion

This paper presents a comprehensive OEE model that accounts for experimental variability of transparent perovskite solar cells for perovskite-based 4T tandem devices. The model comprises a detailed electronic model for the perovskite top cell and an equivalent-circuit-based model for the bottom cell. Focus is on the perovskite layer thickness and how the optical and recombination properties of the solar cell vary when fitted with the OEE model.

After calibration and validation with in-house fabricated devices, the optical and recombination parameters were fitted and their functional form captured with piecewise cubic Hermite interpolating polynomials. Our results suggest that there is a significant deviation in the optical and recombination properties as
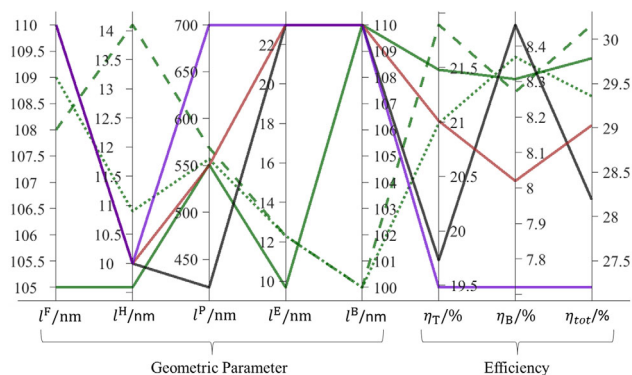
Figure 8. Optimal parameter values from the OEE model [Green: from fitting the best (--), median (—) and worst (:) performing cells] compared with in-house fabricated parameters represented by black, red, and purple lines for tandem device with top perovskite solar cell with 420, 550, and 700 nm perovskite layer thickness, respectively.

the layer thickness of the perovskite increases: the bulk recombination rate in the perovskite layer increases by almost two orders of magnitude when its layer thickness increases from 420 to 700 nm; the interface recombination increases significantly by a factor of near-to three at the interface II with the rougher side due to poor conformity with the electron transport layer while at interface III, the recombination rate decreases by one order of magnitude; and the optical constants for thicker perovskite layers have poorer light absorption, which could be due to poorer perovskite crystal quality when spin-coated on the hole transport layer. A multiparametric optimization study conducted on the layer thicknesses in the top perovskite cell predicts improving the tandem device efficiency to 30.3% by reducing the electron transporting and back contact electrode layers and keeping the perovskite layer thickness at around 550 nm.

The proposed methodology can be further improved to include more perovskite layer thicknesses to provide more data to obtain a polynomial functional form to better describe the optical and recombination properties. Furthermore, one can consider varying more factors such as the layer thickness of the other layers in the perovskite solar cell, spin-coating parameters, and bandgap of perovskite layer to obtain a multivariate polynomial functional form to describe the optical and recombination properties. It is advised to consider adopting factorial experiments, when increasing the number of levels and factors, to reduce the number of experiments needed to come to a meaningful conclusion.

Furthermore, our results suggest that it would be beneficial to explore fabrication methods that maintain high film quality at a perovskite layer thickness of around 700 nm to improve the tandem-device efficiency. In addition, we also recommend studying the optical losses that occur at the interfaces between the top and bottom cells, a known drawback of the 4T configuration.

The OEE model can be applied to other 4T device architectures—for example, all-perovskite, perovskite on organic, and perovskite on silicon. Furthermore, a multiparametric optimization study considering the other geometric parameters could be carried out to further identify pathways that improve performance.

4. Experimental Section

Numerics for the OEE Model: The mathematical model was implemented in the commercial software COMSOL MULTIPHYSICS 5.2a (electronics) and MATLAB R2021b (optics and electrics).

We adopted the general transfer matrix method to account for the optical interference effects from the thin coherent layers and the absorption of light due to the thick incoherent glass layers.[40] The front incident light follows AM1.5 ASTM G-173-03 standard spectrum.

Both electron and hole fluxes were calculated with Lagrange multipliers with weak constraints set at interfaces I and IV to determine the interface charge carrier fluxes.

The computational domains were resolved with around 6200 elements to ensure mesh independent solutions. One complete simulation for a tandem device took around 5 s (wall-clock time) on a workstation with an eight-core 2.90 GHz processor and 16.0 GB RAM.

Calibration and Validation: The optical constants to simulate the different layers in the tandem device are shown in **Figure 9**, and the remaining input parameters are compiled in Table 3. Overall, six parameters were fitted with experimentally measured current–voltage characteristics from the champion in-house perovskite cells. These parameters were calibrated by solving a nonlinear curve-fitting problem with genetic algorithm in MATLAB R2021b, i.e., finding the parameters

$$\Phi_T = (A_{e,h}^P, B_{rad}^P, \tau_{e,h}^P, \nu_{II}, \nu_{III}, \xi) \tag{1}$$

$$\Phi_B = (i_{01}, i_{02}, R_s, R_{sh}) \tag{2}$$
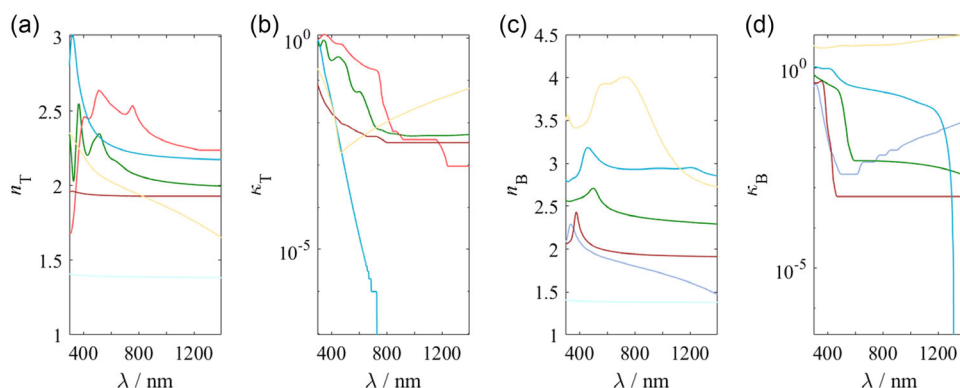
Figure 9. a,c) Refractive indices and b,d) extinction coefficients for the subcells. The color of the lines corresponds to the layers in Figure 1a.[18,53–60]

that best fit the expression

$$\min_{\phi_T} \left\| i_T(\phi_T, V_a) - i_{exp}(V_a) \right\|^2 \quad (3)$$

$$\min_{\phi_B} \left\| i_B(\phi_B, V_a) - i_{exp}(V_a) \right\|^2 \quad (4)$$

where $i_{T,B}$ and i_{exp} are vectors that contain the simulated and experimentally measured current densities at various applied voltages, respectively.

In addition, for the bottom electric model, we calibrated four diode parameters with the methodology proposed by Sulyok and Summhammer.[41]

The piecewise cubic hermite interpolating polynomial is expressed as

$$f(l^P) = \begin{cases} c_1 l^{P3} + c_2 l^{P2} + c_3 l^P + c_4, & 420\,nm \leq l^P \leq 550\,nm \\ c_5 l^{P3} + c_6 l^{P2} + c_7 l^P + c_8, & 550\,nm \leq l^P \leq 700\,nm \end{cases} \quad (5)$$

where c is the fitted parameter and $f = (A, B, \tau, \nu_{II}, \nu_{III}, \xi)$ is the function. The fitted parameters are compiled in **Table 4**.

Optimization: The optimization problem is defined as

$$\text{maximize } \eta_{tot} \quad (6)$$

Subject to the following bounds

$$100\,nm \leq l_T^E \leq 350\,nm$$
$$5\,nm \leq l_T^H \leq 60\,nm$$
$$420\,nm \leq l_T^P \leq 700\,nm \quad (7)$$
$$5\,nm \leq l_T^E \leq 30\,nm$$
$$100\,nm \leq l_T^B \leq 350\,nm$$

The hyperparameters for the genetic algorithm in MATLAB was set to 100 for population size, 0.7 for crossover fraction, and 5 elite counts.

Materials: Lead iodide (99.99%), lead bromide (>98.0%), and [4-(3,6-dimethyl-9 H-carbazol-9-yl)butyl]phosphonic acid (Me-4PACz, >99.0%) were purchased from TCI. Formamidinium iodide (>99.99%), methylammonium bromide (>99.99%), and phenethylammonium iodide were purchased from Greatcell Solar Materials. Cesium iodide (99.9%), rubidium iodide (99.9%), nickel(II) nitrate hexahydrate (99.999%), sodium hydroxide (>98%), 2-propanol (IPA, anhydrous, 99.5%), N,N-dimethylformamide (DMF, anhydrous, 99.8%), dimethyl sulfoxide (DMSO, anhydrous, >99.5%), and anisole (anhydrous, 99.7%) were purchased from Sigma Aldrich.

Materials Synthesis: NiO$_x$ nanoparticles was synthesized in house following previously published report.[61] In short, 9 g of nickel(II) nitrate hexahydrate was fully dissolved in 120 mL deionized water, in which 120 mL sodium hydroxide (1 mol mL^{-1}) was added under vigorous stirring at room temperature. The solution was stirred for another 5 min to complete the reaction; the resulted green Ni(OH)$_2$ was collected by centrifugation at 6000 r.p.m. for 8 min, followed by washing with deionized water for a few times until the pH values of the supernatants were neutral. Following with freeze-drying for 48 h to obtain high-quality NiO$_x$ nanoparticles with better crystallinity and smaller particle sizes. Finally, the powders were sintered at 275–280 °C for 2 hrs in a tube furnace (ramping up rate, 2–3°C min^{-1}; ramping down rate, 5°C min^{-1}).

Device Fabrication: For the perovskite cells, the ITO glass substrates were first cleaned with ultrasonicator in soap solution followed by deionized water, acetone, and IPA for 10 min for each step. NiO$_x$ nanoparticle dispersion (10 mg mL^{-1} in H$_2$O) was prepared and spin coated onto the ITO substrate at 3000 r.p.m. for 30 s at ambient conditions. After annealing for 10 min at 120 °C, the samples were transferred into a N$_2$-filled glovebox, and a Me-4PACz self-assembled monolayer solution (1 mg mL^{-1} in IPA) was deposited onto the substrate at 3000 r.p.m. for 30 s, following by annealing for 10 min at 100 °C. The Rb$_{0.05}$Cs$_{0.05}$ [(FA$_{0.83}$MA$_{0.17}$)]$_{0.9}$Pb(I$_{0.83}$Br$_{0.17}$)$_3$ perovskite precursor solution was prepared by mixing PbI$_2$, PbBr$_2$, FAI, MABr, CsI, and RbI in DMF/DMSO (4:1) with 1.5 M concentration. The dissolved perovskite solution was spin-coated at 4000 r.p.m. for 40 s with 250 mL antisolvent dropping at

Table 4. Fitted parameters for the optical and recombination functional forms for the best (B), median (M), and worst (W) performing cells with the units left out for readability.

f	Cell	c_1	c_2	c_3	c_4	C_5	c_6	c_7	c_8
$A_{e,h}^P$	B	−1.072e-47	1.769e-44	−9.731e-42	1.914e-39	−4.514e-47	9.724e-44	−6.599e-41	1.452e-38
	M	1.110e-47	−1.86e-44	9.673e-42	−1.219e-39	8.339e-48	−1.943e-44	1.309e-41	−2.389e-39
	W	6.859e-48	−2.571e-44	2.206e-41	−5.007e-39	5.152e-48	−2.622e-44	2.417e-41	−5.730e-39
B_{rad}^P	B	−2.012e-28	8.116e-25	−5.753e-22	1.25432e-19	−9.891e-25	2.1005e-21	−1.4127e-18	3.062081e-16
	M	1.2427e-25	−1.5105e-22	5.33813e-20	−4.3045e-18	5.121e-26	−8.4498e-23	4.64739e-20	−8.482341e-18
	W	−1.2083e-26	1.9937e-23	−1.0965e-20	2.0221e-18	−9.6357e-23	2.0458e-19	−1.3759e-16	2.9821e-14
$\tau_{e,h}^P$	B	1.071e-12	−1.926e-9	1.051e-6	−8.4861e-5	4.018e-12	−8.829e-9	5.970e-6	−1.1923e-3
	M	1.1561e-13	−1.9076e-10	1.0492e-7	7.6641e-5	1.3088e-11	−2.7801e-8	1.8704e-5	−3.9591e-3
	W	4.8080e-13	−1.0200e-09	6.0238e-07	−1.1643e-05	9.8806e-12	−2.1266e-08	1.4343e-05	−3.0084e-3
ν_{II}	B	−5.636e-36	9.743e-33	−5.603e-30	1.097476e-27	−4.233e-36	1.01637e-32	−7.339e-30	1.6914841e-27
	M	−3.5853e-36	5.916e-33	−3.2537e-30	6.3789e-28	−4.977e-36	1.10332e-32	−7.6197e-30	1.7227e-27
	W	−8.9802e-37	3.3214e-33	−2.8386e-30	7.4504e-28	−6.7452e-37	3.3884e-33	−3.1152e-30	8.3970e-28
ν_{III}	B	1.371e-34	−1.706e-31	6.17581e-29	−3.325e-27	7.406e-36	−8.842e-33	1.492e-30	2.461e-27
	M	1.3648e-33	−1.7406e-30	6.7618e-28	−7.0070e-26	1.748148e-35	−2.8844e-32	1.5864e-29	−5.6148e-28
	W	1.1856e-33	−1.5051e-30	5.7692e-28	−5.5835e-26	1.4074e-36	6.7178e-33	−1.1474e-29	7.4650e-27
ξ	B	−2.685e-9	5.168e-6	−2.578e-3	0.352228	−2.017e-9	5.369e-6	−3.404e-3	0.63521307
	M	1.2000e-11	1.7289e-08	9.2530e-04	−0.4488	9.0134e-12	1.6393e-08	9.2899e-04	−0.4500
	W	−2.1519e-10	1.3134e-08	1.107e-3	−0.4731	−1.6163e-10	2.9202e-08	1.0407e-3	−0.4504

30 s after the spin started. The films were then annealed at 100 °C for 15 min. After cooling to room temperature, 100 mL PEAI solution (1 mg mL^{-1} in IPA) was quickly dropped on the perovskite and spin-coated at 4000 r.p.m. for 30 s and annealed at 100 °C for 10 min. The substrates were then transferred into a thermal evaporator where a 25 nm-thick C$_{60}$ layer was evaporated as the electron transporting layer, following by depositing a 20 nm thick SnO$_x$ as a buffer layer with the atomic layer deposition technique. Finally, 100 nm ITO semi-transparent electrode was sputtered, and 100 nm Ag was evaporated as the top contact. A LiF layer was also evaporated as the anti-reflection coating.

The CIS cell was grown through multistage co-evaporation onto a Mo-coated soda-lime glass substrate. In this process, the constituent metals were co-deposited in a vacuum chamber, at a substrate temperature of maximal 500 °C, leading to the formation of slightly sub-stoichiometric CIS. The absorber was then treated in situ with NaF and RbF in a Se atmosphere. A detailed description of the growth process is given in reference.[36] A subsequent CdS buffer layer of approximately 35 nm was deposited by the chemical bath deposition. In addition, 70 nm nonintentionally doped ZnO was deposited by RF magnetron sputtering. The front contact was realized by sputtering IZO (In$_2$O$_3$:ZnO, 89.3:10.7 wt%) in pulsed DC mode, followed by a Ni/Al current collection grid and a 105 nm MgF$_2$ antireflection coating by e-beam evaporation.

Characterization: J–V measurements were carried out using a Keithley 2400 sourcemeter in an ambient environment at 25 °C and 55% relative humidity. The devices were measured both in reverse scan and forward scan with a 10 mV interval and 10 ms delay time. Illumination was provided by an Abet Sun 2000 solar simulator with AM 1.5G spectrum and light intensity of 100 mW cm^{-2}, which was calibrated by a WPVS reference cell from Fraunhofer ISE. During the J–V measurement, an optical aperture mask (0.055 cm^2) was used to ensure the accurate cell area.

Appendix

Nomenclature

A_i	Auger recombination coefficients for two-i species collisions, m^6 s^{-1}
B_{rad}	Radiative recombination coefficient, m^3 s^{-1}
C	Material cost for a 1 m^2 perovskite cell
c	Speed of light in vacuum, m s^{-1}
$c_{e,t}$	Electron density when the electron Fermi level is equal to the trap level, m^{-3}
$c_{h,t}$	Hole density when the hole Fermi level is equal to the trap level, m^{-3}
c_e	Electron concentration, m^{-3}
c_h	Hole concentration, m^{-3}
c_i	Intrinsic carrier densities, m^{-3}
$c_{i,s}$	Interface concentration of species i in P, m^{-3}
D_i	Diffusion coefficient of species i, m^2 s^{-1}
e	Elementary charge, C
E_i	Intrinsic potential energy, eV
E_t	Energy of trap state, eV
$\mathfrak{F}$	Fill factor
G	Generation rate of electrons and holes, m^{-3} s^{-1}
h	Planck's constant,
I_0	Spectral irradiance of incident light, W m^{-2}
i	Current density, A m^{-2}
j_i	Flux of species i, m^{-2} s^{-1}

k	Wavenumber, m^{-1}
k_B	Boltzmann constant, J K^{-1}
l	Layer thickness, m
n	Refractive index
n	Diode ideality factor
N_c	Effective conduction band density of states, m^{-3}
N_v	Effective valence band density of states, m^{-3}
N_a^{H-}	Ionized acceptor impurity concentration in H, m^{-3}
N_d^{E+}	Ionized donor impurity concentration in E, m^{-3}
p_{in}	Input power density, W m^{-2}
Q	Time average of the energy dissipated per second, J m^{-3} s^{-1}
R_a	Spectral Albedo
R_{Aug}	Auger recombination rate, m^{-3} s^{-1}
R_{rad}	Radiative recombination rate, m^{-3} s^{-1}
R_{SRH}	Shockley–Read–Hall recombination rate, m^{-3} s^{-1}
R^P	Net recombination rate of electrons and holes, m^{-3} s^{-1}
$\overline{R}$	Mean rank
S	Source term
T	Temperature, K
ν	Effective interface-recombination velocity, m^4 s^{-1}
V_a	Applied voltage, V
V_{bi}	Built in voltage, V
V_t	Thermal voltage, V
W	Work function, eV

Greek	
α	Absorption coefficient, m^{-1}
ε_0	Permittivity of free space, F m^{-1}
ε	Permittivity of material, F m^{-1}
ξ	Fitting parameter for perovskite layer optical constants
η_i	Device equivalent efficiency of subcell i
η_{tot}	Tandem device efficiency
κ	Extinction coefficient
μ_i	Mobility of species I, m^2 V^{-1} s^{-1}
μ	Mean
τ_i	SRH recombination lifetime for species I, s
χ_e	Absolute value of electron affinity, eV
χ_h	Absolute value of ionization potential, eV
ψ	Electric potential, V

Superscripts	
B	Back contact electrode
E	Electron-transporting layer
F	Front contact electrode
G	Glass layer
H	Hole-transporting layer
O	Passivating layer
P	Perovskite layer
+	Layer after interface
-	Layer before interface

| ′ | d/dx |
| ′′ | d^2/dx^2 |

Subscripts

B	Bottom cell
e	Electron
h	Hole
mpp	Maximum power point
sc	Short circuit
T	Top cell
tot	Tandem device
I	Interface between contact electrode and electron-transporting layer
II	Interface between electron-transporting layer and perovskite layer
III	Interface between hole-transporting layer and perovskite layer
IV	Interface between contact electrode and hole-transporting layer
V	Interface between air and top cell glass layer
VI	Interface between top cell antireflective coating with bottom cell antireflective coating
VII	Interface between bottom cell contact electrode with bottom cell glass layer

Supporting Information

Supporting Information is available from the Wiley Online Library or from the author.

Conflict of Interest

The authors declare no conflict of interest.

Author Contributions

H.Q.T., E.B., Y.H., and H.X. conceived this work. E.B., Y.H., and H.X. supervised. H.L. fabricated and characterized the perovskite devices. M.K. fabricated the CIS devices. R.K.K. characterized the tandem devices. C.R., A.N.T., and F.F. supervised the experiment for CIS bottom cell. H.Q.T., X.Z., E.B., and H.X. developed the OEE model. H.Q.T. calibrated and validated the OEE model. All authors discussed the results. H.Q.T. and H.L. wrote the manuscript with input from all authors.

Data Availability Statement

The data that support the findings of this study are available from the corresponding author upon reasonable request.

[1] Z. Wang, X. Zhu, S. Zuo, M. Chen, C. Zhang, C. Wang, X. Ren, Z. Yang, Z. Liu, X. Xu, Q. Chang, S. Yang, F. Meng, Z. Liu, N. Yuan, J. Ding, S. F. Liu, D. Yang, *Adv. Funct. Mater.* **2020**, *30*, 1908298.

[2] T. Duong, H. Pham, T. C. Kho, P. Phang, K. C. Fong, D. Yan, Y. Yin, J. Peng, M. A. Mahmud, S. Gharibzadeh, B. A. Nejand, I. M. Hossain, M. R. Khan, N. Mozaffari, Y. Wu, H. Shen, J. Zheng, H. Mai, W. Liang, C. Samundsett, M. Stocks, K. Mcintosh, G. G. Andersson, U. Lemmer, B. S. Richards, U. W. Paetzold, A. Ho-Ballie, Y. Liu, D. Macdonald, A. Blakers, et al., *Adv. Energy Mater.* **2020**, *10*, 1903553.

[3] M. Jiang, Y. Kang, T. Sewastianik, J. Wang, H. Tanton, K. Alder, P. Dennis, Y. Xin, Z. Wang, R. Liu, M. Zhang, Y. Huang, M. Loda, A. Srivastava, R. Chen, M. Liu, R. D. Carrasco, *Nat. Commun.* **2020**, *11*, https://doi.org/10.1038/s41467-020-15077-3.

[4] A. Rohatgi, K. Zhu, J. Tong, D. H. Kim, E. Reichmanis, B. Rounsaville, V. Prakash, Y.-W. Ok, *IEEE J. Photovoltaics* **2020**, *10*, 417.

[5] R. Lin, K. Xiao, Z. Qin, Q. Han, C. Zhang, M. Wei, M. I. Saidaminov, Y. Gao, J. Xu, M. Xiao, A. Li, J. Zhu, E. H. Sargent, H. Tan, *Nat. Energy* **2019**, *4*, 864.

[6] D. Zhao, C. Wang, Z. Song, Y. Yu, C. Chen, X. Zhao, K. Zhu, Y. Yan, *ACS Energy Lett.* **2018**, *3*, 305.

[7] J. Tong, Z. Song, D. H. Kim, X. Chen, C. Chen, A. F. Palmstrom, P. F. Ndione, M. O. Reese, S. P. Dunfield, O. G. Reid, J. Liu, F. Zhang, S. P. Harvey, Z. Li, S. T. Christensen, G. Teeter, D. Zhao, M. M. Al-Jassim, M. F. A. M. Van Hest, M. C. Beard, S. E. Shaheen, J. J. Berry, Y. Yan, K. Zhu, *Science* **2019**, *364*, 475.

[8] R. Lin, J. Xu, M. Wei, Y. Wang, Z. Qin, Z. Liu, J. Wu, K. Xiao, B. Chen, S. M. Park, G. Chen, H. R. Atapattu, K. R. Graham, J. Xu, J. Zhu, L. Li, C. Zhang, E. H. Sargent, H. Tan, *Nature* **2022**, *603*, 73.

[9] T. Feurer, R. Carron, G. Torres Sevilla, F. Fu, S. Pisoni, Y. E. Romanyuk, S. Buecheler, A. N. Tiwari, *Adv. Energy Mater.* **2019**, *9*, 1901428.

[10] C. Zhang, M. Chen, F. Fu, H. Zhu, T. Feurer, W. Tian, C. Zhu, K. Zhou, S. Jin, S. M. Zakeeruddin, A. N. Tiwari, N. P. Padture, M. Grätzel, Y. Shi, *Energy Environ. Sci.* **2022**, *15*, 1536.

[11] C. U. Kim, J. C. Yu, E. D. Jung, I. Y. Choi, W. Park, H. Lee, I. Kim, D.-K. Lee, K. K. Hong, M. H. Song, K. J. Choi, *Nano Energy* **2019**, *60*, 213.

[12] M. Jošt, E. Köhnen, A. Al-Ashouri, T. Bertram, Š. Tomšič, A. Magomedov, E. Kasparavicius, T. Kodalle, B. Lipovšek, V. Getautis, R. Schlatmann, C. A. Kaufmann, S. Albrecht, M. Topič, *ACS Energy Lett.* **2022**, *7*, 1298.

[13] H. Shen, T. Duong, J. Peng, D. Jacobs, N. Wu, J. Gong, Y. Wu, S. K. Karuturi, X. Fu, K. Weber, X. Xiao, T. P. White, K. Catchpole, *Energy Environ. Sci.* **2018**, *11*, 394.

[14] Q. Han, Y.-T. Hsieh, L. Meng, J.-L. Wu, P. Sun, E.-P. Yao, S.-Y. Chang, S.-H. Bae, T. Kato, V. Bermudez, Y. Yang, *Science* **2018**, *361*, 904.

[15] M. Mousa, F. Z. Amer, R. I. Mubarak, A. Saeed, *Optik* **2022**, *251*, 168458.

[16] A. Kumar, S. Singh, M. K. A. Mohammed, A. E. Shalan, *Eur. J. Inorg. Chem.* **2021**, *2021*, 4959.

[17] X. Zhao, H. Q. Tan, E. Birgersson, H. Xue, *Sol. Energy* **2022**, *231*, 716.

[18] S. Manzoor, J. Häusele, K. A. Bush, A. F. Palmstrom, J. Carpenter, Z. J. Yu, S. F. Bent, M. D. Mcgehee, Z. C. Holman, *Opt. Express* **2018**, *26*, 27441.

[19] R. Hosseinian Ahangharnejhad, A. B. Phillips, K. Ghimire, P. Koirala, Z. Song, H. M. Barudi, A. Habte, M. Sengupta, R. J. Ellingson, Y. Yan, R. W. Collins, N. J. Podraza, M. J. Heben, *Sustainable Energy Fuels* **2019**, *3*, 1841.

[20] N. Tucher, O. Höhn, J. N. Murthy, J. C. Martinez, M. Steiner, A. Armbruster, E. Lorenz, B. Bläsi, J. C. Goldschmidt, *Opt. Express* **2019**, *27*, A1419.

[21] E. Raoult, R. Bodeux, S. Jutteau, S. Rives, A. Yaiche, A. Blaizot, D. Coutancier, J. Rousset, S. Collin, *Opt. Express* **2022**, *30*, 9604.

[22] M. Filipič, P. Löper, B. Niesen, S. De Wolf, J. Krč, C. Ballif, M. Topič, *Opt. Express* **2015**, *23*, A263.

[23] A. Rolland, L. Pedesseau, M. Kepenekian, C. Katan, Y. Huang, S. Wang, C. Cornet, O. Durand, J. Even, *Opt. Quantum Electron.* **2018**, *50*, https://doi.org/10.1016/j.xcrp.2022.101038.

[24] H. Q. Tan, X. Zhao, E. Birgersson, F. Lin, H. Xue, *Sol. Energy* **2021**, *216*, 589.

[25] R. Pandey, S. Sharma, J. Madan, R. Sharma, *J. Micromech. Microeng.* **2022**, *32*, 014004.

[26] M. Soldera, A. Koffman-Frischknecht, K. Taretto, *J. Phys. D: Appl. Phys.* **2020**, *53*, 315104.

[27] X. Zhao, H. Q. Tan, E. Birgersson, W. Chen, Y. Hou, H. Xue, *Cell Rep. Phys. Sci.* **2022**, *3*, 101038.

[28] N. Singh, A. Agarwal, M. Agarwal, *Sol. Energy* **2020**, *208*, 399.

[29] H. Q. Tan, X. Zhao, A. Jiao, E. Birgersson, H. Xue, *Sol. Energy* **2022**, *231*, 1092.

[30] J. M. Ball, S. D. Stranks, M. T. Hörantner, S. Hüttner, W. Zhang, E. J. W. Crossland, I. Ramirez, M. Riede, M. B. Johnston, R. H. Friend, H. J. Snaith, *Energy Environ. Sci.* **2015**, *8*, 602.

[31] S. Brittman, E. C. Garnett, *J. Phys. Chem. C* **2016**, *120*, 616.

[32] D. Zhao, Y. Yu, C. Wang, W. Liao, N. Shrestha, C. R. Grice, A. J. Cimaroli, L. Guan, R. J. Ellingson, K. Zhu, X. Zhao, R.-G. Xiong, Y. Yan, *Nat. Energy* **2017**, *2*, 17018.

[33] T. Du, W. Xu, S. Xu, S. R. Ratnasingham, C.-T. Lin, J. Kim, J. Briscoe, M. A. Mclachlan, J. R. Durrant, *J. Mater. Chem. C* **2020**, *8*, 12648.

[34] M. Mujahid, C. Chen, J. Zhang, C. Li, Y. Duan, *InfoMat* **2021**, *3*, 101.

[35] S. Rahmany, L. Etgar, *ACS Energy Lett.* **2020**, *5*, 1519.

[36] B. Werner, W. Kołodenny, M. Prorok, A. Dziedzic, T. Żdanowicz, *Sol. Energy Mater. Sol. Cells* **2011**, *95*, 2583.

[37] B. L. Williams, S. Smit, B. J. Kniknie, K. J. Bakker, W. Keuning, W. M. M. Kessels, R. E. I. Schropp, M. Creatore, *Prog. Photovoltaics Res. Appl.* **2015**, *23*, 1516.

[38] U. Malm, M. Edoff, *Prog. Photovoltaics Res. Appl.* **2008**, *16*, 113.

[39] D. Liu, M. K. Gangishetty, T. L. Kelly, *J. Mater. Chem. A* **2014**, *2*, 19873.

[40] C. C. Katsidis, D. I. Siapkas, *Appl. Opt.* **2002**, *41*, 3978.

[41] G. Sulyok, J. Summhammer, *Energy Sci. Eng.* **2018**, *6*, 424.

[42] Z. Berkai, M. Daoudi, N. Mendil, A. Belghachi, *Phys. Lett. A* **2019**, *383*, 2090.

[43] A. Kumar, A. Priyadarshi, S. Shukla, M. Manjappa, L. J. Haur, S. G. Mhaisalkar, R. Singh, *J. Appl. Phys.* **2018**, *124*, https://doi.org/10.1063/1.5016829.

[44] H. S. Kim, C. K. Kim, *Mol. Cryst. Liq. Cryst.* **2019**, *678*, 33.

[45] F. Yang, D.-W. Kang, Y.-S. Kim, *RSC Adv.* **2017**, *7*, 19030.

[46] Z. Qiu, H. Gong, G. Zheng, S. Yuan, H. Zhang, X. Zhu, H. Zhou, B. Cao, *J. Mater. Chem. C* **2017**, *5*, 7084.

[47] J.-C. Ke, Y.-H. Wang, K.-L. Chen, P.-H. Huang, C.-J. Huang, *Int. J. Photoenergy* **2013**, *2013*, https://doi.org/10.1002/adom.202101553.

[48] M. Deepa, M. Salado, L. Calio, S. Kazim, S. M. Shivaprasad, S. Ahmad, *Phys. Chem. Chem. Phys.* **2017**, *19*, 4069.

[49] A. Singh, A. Gagliardi, *Sol. Energy* **2019**, *187*, 39.

[50] T. Golubev, D. Liu, R. Lunt, P. Duxbury, **2019**, *AIP Adv. 9*, 035026.

[51] M. Bruzzi, N. Falsini, N. Calisi, A. Vinattieri, *Energies* **2020**, *13*, 1643.

[52] S. Prathapani, P. Bhargava, S. Mallick, *Appl. Phys. Lett.* **2018**, *112*, 92104.

[53] M. R. Vogt, H. Hahn, H. Holst, M. Winter, C. Schinke, M. Kontges, R. Brendel, P. P. Altermatt, *IEEE J. Photovoltaics* **2016**, *6*, 111.

[54] Z. C. Holman, M. Filipič, A. Descoeudres, S. De Wolf, F. Smole, M. Topič, C. Ballif, *J. Appl. Phys.* **2013**, *113*, 13107.

[55] D. Koushik, M. Jošt, A. Dučinskas, C. Burgess, V. Zardetto, C. Weijtens, M. A. Verheijen, W. M. M. Kessels, S. Albrecht, M. Creatore, *J. Mater. Chem. C* **2019**, *7*, 12532.

[56] A. Tejada, S. Peters, A. Al-Ashouri, S. H. Turren-Cruz, A. Abate, S. Albrecht, F. Ruske, B. Rech, J. A. Guerra, L. Korte, *Adv. Opt. Mater.* **2022**, *10*, 2101553.

[57] E. Çetinörgü, C. Gümüş, S. Goldsmith, F. Mansur, *Phys. Status Solidi A* **2007**, *204*, 3278.

[58] H. H. Moore, *J. Phys. Chem. Ref. Data* **1982**, *9*, 161.

[59] R. Carron, E. Avancini, T. Feurer, B. Bissig, P. A. Losio, R. Figi, C. Schreiner, M. Bürki, E. Bourgeois, Z. Remes, M. Nesladek, S. Buecheler, A. N. Tiwari, *Sci. Technol. Adv. Mater.* **2018**, *19*, 396.

[60] S. Minoura, T. Maekawa, K. Kodera, A. Nakane, S. Niki, H. Fujiwara, *J. Appl. Phys.* **2015**, *117*, https://doi.org/10.1063/1.5068690.

[61] W. Chen, Y. Zhu, J. Xiu, G. Chen, H. Liang, S. Liu, H. Xue, E. Birgersson, J. W. Ho, X. Qin, J. Lin, R. Ma, T. Liu, Y. He, A. M.-C. Ng, X. Guo, Z. He, H. Yan, A. B. Djurišić, Y. Hou, *Nat. Energy* **2022**, *7*, 229.

2300339 (13 of 13)